Solar Phys (2010) 262: 495–509
DOI 10.1007/s11207-010-9536-1

SOLAR IMAGE PROCESSING AND ANALYSIS

Dynamic Three-Dimensional Tomography of the Solar Corona

M.D. Butala · R.J. Hewett · R.A. Frazin · F. Kamalabadi

Received: 18 May 2009 / Accepted: 18 February 2010 / Published online: 10 March 2010

Abstract Empirical, three-dimensional electron-density maps of the solar corona can be tomographically reconstructed using polarized-brightness images measured from ground- and space-based observatories. Current methods for computing these reconstructions require the assumption that the structure of the corona is unchanging with time. We present the first global reconstructions that do away with this static assumption and, as a result, allow for a more accurate empirical determination of the dynamic solar corona. We compare the new dynamic reconstructions of the coronal density during February 2008 to a sequence of static reconstructions. We find that the new dynamic reconstructions are less prone to certain computational artifacts that may plague the static reconstructions. In addition, these benefits come without a significant increase in computational cost.

Keywords Corona · Tomography · Statistical image processing

1. Introduction

The dynamic physical processes that heat the corona and drive the solar wind are not completely understood (Aschwanden, 2004). Empirical estimates of plasma parameters, such

---

Solar Image Processing and Analysis
Guest Editors: J. Ireland and C.A. Young

M.D. Butala (✉) · R.J. Hewett · F. Kamalabadi
University of Illinois at Urbana-Champaign, Champaign, IL, USA
e-mail: butala@illinois.edu

R.J. Hewett
e-mail: rhewett2@illinois.edu

F. Kamalabadi
e-mail: farzadk@illinois.edu

R.A. Frazin
University of Michigan, Ann Arbor, MI, USA
e-mail: rfrazin@umich.edu

as temperature and electron density, can provide insight into these processes (Cohen *et al.*, 2007; Vásquez *et al.*, 2008). Solar tomography (Davila, 1994; Frazin and Kamalabadi, 2005) has been used to reconstruct the global three-dimensional (3D) structure of the corona based on observations. In this paper, the electron density is reconstructed in a dynamic estimation framework that moves away from the static assumption made in prior work (Butala *et al.*, 2008). These improved estimates will provide a more complete view of the dynamic electron-density distribution, which will, in turn, contribute to a better physical picture of the corona.

For electron-density reconstruction, the inputs to solar tomography are images of polarized brightness (pB), which are routinely measured by coronagraphs. Each pixel of each pB image is proportional to the electron density integrated along the pixel's line-of-sight through the optically thin corona. A tomographic reconstruction of the electron density combines pB images from multiple points of view, ideally spanning 180° about the Sun, to resolve the depth ambiguity resulting from the line-of-sight integration. Distinct points of view are provided by solar rotation (the Sun has a synodic rotation period of 27.3 days) and spatially separated sensors, such as those provided by the *Solar and Terrestrial Relations Observatory* (STEREO: Kaiser *et al.*, 2007).

The coronal electron density was first empirically determined by van de Hulst (1950) under the assumption of azimuthal symmetry and a power-law parametrization. With subsequent advancements in computational resources, such simplifying assumptions are no longer necessary and 3D estimates of the coronal electron density are now routinely computed; see *e.g.* Butala, Frazin, and Kamalabadi (2005) or Kramar *et al.* (2009) for examples of such 3D reconstructions and Frazin and Kamalabadi (2005) for a recent review of solar tomography including references to contemporary work. However, existing methods for recovering the global 3D coronal electron density assume that the structure of the corona is static over the measurement interval and significant changes in the corona can result in reconstruction artifacts (Butala, Frazin, and Kamalabadi, 2005; Frazin and Kamalabadi, 2005). Prior to STEREO, a full 180° view of the corona required nearly 14 days of observation. Three simultaneous view points (from the Earth and the two STEREO satellites, each separated by 60° from the Earth) can reduce the measurement interval to less than five days, although the corona can change significantly at even shorter time scales.

In this paper, we show the first time-dependent 3D estimates, *i.e.* 4D estimates, of the electron density based on our recently developed dynamic tomography framework (Butala *et al.*, 2008, 2009). Time-dependent tomography of solar-wind parameters was explored by Dunn *et al.* (2005). Four-dimensional reconstruction of solar plumes has been considered in Barbey *et al.* (2008), but this work differs in that we reconstruct the global 4D electron density structure of the global corona. The electron-density reconstructions are based on individual STEREO coronagraph measurements, and, to our knowledge, Kramar *et al.* (2009) present the only other solar tomography work that uses such data. The dynamic estimates are compared to a sequence of static electron-density reconstructions based on a sliding measurement time window. The results demonstrate that the dynamic electron-density estimates have a smaller residual and fewer reconstruction artifacts when compared to the static estimates. Additionally, we find that the dynamic reconstruction algorithm is less computationally demanding than creating a sequence of windowed static electron-density estimates.

The remainder of the paper is organized as follows: first, the time period of interest, instrumental details, and data prepossessing procedures are given in Section 2. Then the static and dynamic tomographic reconstruction methods are described in Section 3. Next, Section 4 presents the static and dynamic electron-density reconstructions to demonstrate the potential of our new methods. Conclusions and potential extensions of our work are given in Section 5.

2. Observations

Data for the dynamic coronal-density reconstructions are acquired from the COR1 coronagraph (Thompson *et al.*, 2003), the innermost coronagraph within the SECCHI instrument package (Howard *et al.*, 2008), onboard the dual STEREO spacecraft. We will henceforth use COR1A to refer to the COR1 coronagraph on the Ahead satellite, and likewise COR1B will henceforth refer to the COR1 coronagraph on the Behind satellite. The COR1 coronagraphs have a field of view of $1.3-4R_{\odot}$. We use data from $1.5-3R_{\odot}$ to form the electron-density reconstructions in Section 4. The lower radius is restricted to avoid systematic instrumental diffraction clearly visible in the COR1 images and is the same as the lower radius chosen in Kramar *et al.* (2009). The upper radius is restricted only to reduce computational costs for this work. Images from polarization angles of 0°, 120°, and 240° are combined to form pB images, calibrated, background subtracted using the SECCHI_PREP (http://sohowww.nascom.nasa.gov/solarsoft/stereo/secchi/doc/secchi_prep.html) IDL routine with the so-called monthly-roll background images. Additionally, the calibration routine applies an intercalibration factor to each COR1A and COR1B image (Thompson and Reginald, 2008). However, we find that the processed COR1 images still contain a few localized outlier values, due most likely to cosmic rays hitting the detectors. We found that the simple rule of discarding COR1 image pixels with values greater than $5 \times 10^{-8} B_{\odot}$ was sufficient to remove all outliers. During the reconstruction process, the images were binned from 1024×1024 to 256×256 pixels to reduce computational costs.

The data used are from the four-week period between 1 February 2008 and 29 February 2008 of Carrington Rotation (CR) numbers 2066 and 2067. This time period was chosen because it is close to a monthly calibration roll and, as a result, the background subtraction will best remove instrumental scattered light. In addition, we choose this period to compare our results in Section 4 to Kramar *et al.* (2009) who also consider CR 2066. During this time period, the spacecraft were separated by approximately 45°. The data set used in this study consists of four images per instrument, per day. The images used were spaced evenly, every six hours. The acquisition times are 00:05:00 UTC, 06:05:00 UTC, 12:05:00 UTC, and 18:05:00 UTC. If no image is available for a time, that time is skipped. Thus, there are 115 images used in the COR1A data set and 110 used in the COR1B data set.

3. Methods

This section focuses on the static and dynamic electron-density reconstruction methods, beginning with the forward model that establishes the relationship of the 2D COR1A and COR1B observations to the 3D coronal electron density. Then, the static and dynamic methods are discussed in turn. The section concludes with the procedure used to determine additional parameters in the dynamic reconstruction framework.

3.1. The Forward Model

The value of each pixel of a coronal pB image is proportional to the electron density integrated along that pixel's line of site (LOS). The relationship is given by the stochastic integral equation

$$y_{i,k} = C \int_{\mathrm{LOS}} H(\mathbf{s}_{i,k},\, \mathbf{s}_{i,k} + l\theta_{i,k})\, x_i(\mathbf{s}_{i,k} + l\theta_{i,k})\, \mathrm{d}l + v_{i,k}, \tag{1}$$

where the subscript i is the time index, $y_{i,k}$ is the kth pixel in the ith coronagraph image, x_i is the electron-density function, H is the Thompson scattering function (van de Hulst, 1950), l is the distance along the pixel's LOS, $\theta_{i,k}$ is a unit vector in that direction, $\mathbf{s}_{i,k}$ is the vector of minimum distance from the LOS to the Sun's center, *i.e.* the solar impact parameter, and $v_{i,k}$ accounts for measurement noise. Three properties of the coronal electron-density function $[x_i]$ are useful to constrain the reconstructions presented in Section 4: the density is non-negative and varies smoothly both spatially and temporally at the scales considered in this work. In the language of the statistical methods considered in Section 3, these properties serve as prior information to augment the empirical knowledge provided by the measurements.

When x_i is unknown, an approximation can be found by discretizing the domain of x_i and approximating it by a vector of coefficients $[\mathbf{x}_i]$ on the discretized basis. Then, the set of continuous forward model equations is expressed through a system of linear equations,

$$\mathbf{y}_i = \mathbf{H}_i\, \mathbf{x}_i + \varepsilon_i, \tag{2}$$

where $\mathbf{y}_i$ is the m_i-dimensional vector of stacked pixels from the pB image at time index i, $\mathbf{H}_i$, an $m_i \times n$ matrix, is the set of coefficients of the discretized form of Equation (1) found by integrating H across the discretized domain, and ε_i is the corresponding noise parameter. For this paper, the physical domain on which x_i is defined is discretized into a spherical grid with uniform spacing in radius, azimuth, and zenith. The discrete form of x_i is then the n-vector $\mathbf{x}_i$ where each element of the vector corresponds to a single cell or voxel in the discretized domain.

3.2. The Static Model

A tomographic inversion of the measured data requires 180° of angular coverage. Solar tomography allows for the full 180° of coverage by exploiting the Sun's rotation. With a single viewpoint (one telescope), 13.7 days of observations are sufficient. Let the number of images in that 13.7 day window be T, and assume that all T images are processed and transformed into their respective linear systems, *i.e.* Equation (2). If the assumption is made that the Sun is not time-varying over that 13.7 day window, *i.e.* the Sun is static over that time period, then the equations for the discretized linear model can be "stacked" together to yield the static linear model for the electron density at time index T,

$$\tilde{\mathbf{y}}_T = \begin{bmatrix} \mathbf{y}_1 \\ \vdots \\ \mathbf{y}_T \end{bmatrix} = \begin{bmatrix} \mathbf{H}_1 \\ \vdots \\ \mathbf{H}_T \end{bmatrix} \mathbf{x}_T + \begin{bmatrix} \varepsilon_1 \\ \vdots \\ \varepsilon_T \end{bmatrix} = \tilde{\mathbf{H}}_T\, \mathbf{x}_T + \tilde{\varepsilon}_T, \tag{3}$$

where $\tilde{\mathbf{y}}_T$ and $\tilde{\varepsilon}_T$ are m-dimensional vectors and $\tilde{\mathbf{H}}_T$ is an $m \times n$ matrix, with

$$m = \sum_{i=1}^{T} m_i. \tag{4}$$

Another way to view the static assumption is that under this model we can reconstruct density information only for the components that vary on time scales longer than 13.7 days. In this paper, static reconstructions are computed by solving the constrained regularized least squares problem

$$\hat{\mathbf{x}}_T^{\mathrm{S}} = \arg\min_{\mathbf{x}\geq\mathbf{0}} \|\tilde{\mathbf{y}}_T - \tilde{\mathbf{H}}_T\,\mathbf{x}\|_2^2 + \lambda\|\mathbf{D}\,\mathbf{x}\|_2^2, \tag{5}$$

where the second term is a regularization function that enforces smoothness on the solution (Butala, Frazin, and Kamalabadi, 2005), λ is referred to as the regularization parameter, and $\mathbf{D}$ is the matrix representation of a gradient operator. The superscript S indicates that $\hat{\mathbf{x}}_T^{\mathrm{S}}$ is the static estimate of the electron density at time index T. Note that the static reconstructions utilize the spatial smoothness and non-negativity prior knowledge as indicated by the inclusion of the spatial regularizer and the constraint in Equation (5).

3.3. The Dynamic Model

The static assumption is a significant drawback of the previous model. Clearly, the solar atmosphere is time-varying over periods shorter than 13.7 days (even during solar minimum), and it is desirable to reconstruct features that vary over these shorter time scales. As the static model is insufficient for these tasks, a more flexible dynamic linear model is used. This model, called the state-space model, consists of two equations:

$$\mathbf{y}_i = \mathbf{H}_i\,\mathbf{x}_i + \varepsilon_i, \tag{6}$$

$$\mathbf{x}_{i+1} = \mathbf{F}_i\,\mathbf{x}_i + \nu_i, \tag{7}$$

called the measurement Equation (6) and the model evolution Equation (7). The terms of Equation (6) are defined in the same way as Equation (2). The second equation captures the underlying dynamics in the process being estimated (*e.g.*, the solar corona). The matrix $\mathbf{F}_i$ captures the physical processes that cause the underlying quantity (*e.g.*, electron density) to vary between time indices i and $i+1$. The random vector ν_i models the inexactness in the linear approximation $\mathbf{F}_i$ and any component of the dynamic evolution that is considered stochastic. The random vectors ε_i and ν_i are mean zero and have covariance matrices $\mathbf{R}_i$ and $\mathbf{Q}_i$, respectively. A spatial regularizer was added to the dynamic approach by augmenting the measurement model Equation (6) with a gradient operator $\mathbf{D}$ in the same manner as by Johns and Mandel (2008) and Butala *et al.* (2009). Ultimately, the linear dynamic model utilizes both spatial and temporal smoothness prior information.

Typically, solutions to problems posed in the state-space framework are estimated using the well-known Kalman filter (KF: Kalman, 1960; Kailath, Sayed, and Hassibi, 2000).[1] While the KF is optimal in the sense that it produces the linear estimate that minimizes the mean-squared error between the true state and the estimate, it is computationally intractable for problems of the scale desired. For a problem with $n \approx 2.1 \times 10^6$ (a cube with sizes of length 128), storage alone of the error covariance matrix $\mathbf{P}_{i|j}$ requires 8 TB of memory. To make this process more feasible, the KF is approximated by the ensemble Kalman filter

---

[1] In the KF literature, estimates are subscripted with two time indices, *e.g.*, $\hat{\mathbf{x}}_{i|j}$. In this notation, i indicates the time index of the estimate and j indicates the time index of the most current data used. For example, the posterior estimate $[\hat{\mathbf{x}}_{i|i}]$ is an estimate at time index i that has assimilated all measurements through time index i. The estimator error covariance matrices $[\mathbf{P}_{i|j}]$ are also written in this notation. $\mathbf{P}_{i|j}$ is defined as the covariance matrix of the error vector $\hat{\mathbf{e}}_{i|j} = \hat{\mathbf{x}}_{i|j} - \mathbf{x}_i$.

(EnKF) (Evensen, 1994; Butala *et al.*, 2008, 2009). The idea behind the EnKF is that rather than maintain the error covariance matrix, process an ensemble of L samples, $\{\tilde{\mathbf{x}}^1_{i|j}, \ldots, \tilde{\mathbf{x}}^L_{i|j}\}$, of the estimate $\hat{\mathbf{x}}_{i|j}$ such that the sample mean,

$$\tilde{\mathbf{x}}_{i|j} = \frac{1}{L}\sum_{l=1}^{L} \tilde{\mathbf{x}}^l_{i|j}, \tag{8}$$

and sample error covariance,

$$\tilde{\mathbf{P}}_{i|j} = \frac{1}{L-1}\sum_{l=1}^{L} \left(\tilde{\mathbf{x}}^l_{i|j} - \tilde{\mathbf{x}}_{i|j}\right)\left(\tilde{\mathbf{x}}^l_{i|j} - \tilde{\mathbf{x}}_{i|j}\right)^T, \tag{9}$$

approximate the KF estimate $[\hat{\mathbf{x}}_{i|j}]$ and the KF error covariance $[\mathbf{P}_{i|j}]$. Storage of and computation on the L samples can have significant computational savings over the classical KF, with little loss in estimate quality (Butala *et al.*, 2009). Theoretical considerations, such as the asymptotic convergence of the EnKF *versus* ensemble size L, are addressed in Butala *et al.* (2009). We will henceforth refer to the dynamic estimate at time index T with the symbol $\hat{\mathbf{x}}^{\mathrm{D}}_T = \tilde{\mathbf{x}}_{T|T}$ where the D superscript indicates a dynamic estimate.

In both the KF and the EnKF, an initial prior estimate $[\mathbf{x}_0]$ and error covariance $[\mathbf{\Pi}_0]$ are required to start the recursion. These parameters are discussed further in Section 3.4. The EnKF algorithm, for T time indices, is given in Algorithm 1.

The function IID_SAMPLE() is a call to a routine that produces independent and identically distributed (i.i.d.) random samples from the provided distribution (*i.e.*, IID_SAMPLE() is a pseudo random number generator) and N indicates the normal distribution. The brackets in lines 3, 13, and 20 of Algorithm 1 denote the formation of a matrix ($\mathbf{X}$, $\mathbf{Y}$, and $\mathbf{U}$, respectively) whose columns are the i.i.d. sample vectors generated in the previous step. In Line 9, the matrix $\mathbf{C}$ is a covariance localization matrix required for algorithmic stability discussed separately in Section 3.4. Also, the $\circ$ operator is the Hadamard, or element-by-element, matrix product. In Line 15, $\mathbf{X}_{:,l}$ is the lth column of the matrix $\mathbf{X}$.

3.4. Model Parameter Selection

The dynamic model of Section 3.3 includes a measurement and state-noise covariance matrices $\mathbf{R}_i$ and $\mathbf{Q}_i$, the mean of the initial state $\mathbf{x}_0$, the initial-state error covariance $\mathbf{\Pi}_0$, the state dynamic model $\mathbf{F}_i$, and the covariance-taper matrix $\mathbf{C}$. The operational procedure used to choose each of these model parameters is described below.

First, we use the state transition model $\mathbf{F}_i = \mathbf{I}$, where $\mathbf{I}$ is the identity matrix, which results in a purely random-walk evolution model for the electron density. The model is often used in practice when a better temporal dynamic model is not known (Zhang, Ghodrati, and Brooks, 2005), and although it is simple, a dynamic tomographic reconstruction with a random-walk model may be superior to a static reconstruction (Frazin *et al.*, 2005). Ideally, we would incorporate nonlinear magnetohydrodynamics into the state transition operator $\mathbf{F}_i$. Such an approach would require the joint estimation of the energy density, velocity, temperature, and magnetic field in addition to electron density, greatly increasing the dimensionality of the already huge problem (Butala *et al.*, 2008). Also, the dynamic reconstruction algorithm in Section 3.3 cannot handle nonlinear operators, although methods do exist for adapting the EnKF to such problems (Evensen, 2003). Incorporating a more sophisticated dynamic model into our dynamic reconstruction framework is ongoing research.

The covariance-taper matrix [$\mathbf{C}$] trades off some bias in the dynamic estimates for a reduction in computational effort as discussed by Butala *et al.* (2009). Several choices for the taper matrix were considered on a lower-resolution reconstruction grid. We found that the electron density reconstructed with the taper matrix $\mathbf{C}=\mathbf{I}$, which results in the greatest reduction in computational effort and largest additional bias, was comparable to the electron densities reconstructed with non-diagonal taper matrices.

We assume that the STEREO/SECCHI-COR1 measurement noise is Poisson. A convenient property of a Poisson random variable is that its mean is equal to its variance. We make the common assumption that the mean of the kth measurement at time index i is given by the kth element of $\mathbf{y}_i$. With this choice, the measurement covariance $\mathbf{R}_i$ is a diagonal matrix with the diagonal equal to $\mathbf{y}_i$. This choice does not account for correlations in the measurement noise, but this information, if known, can easily be incorporated into the off-diagonal elements of $\mathbf{R}_i$.

The state noise covariance [$\mathbf{Q}_i$] is constant in time, *i.e.*, $\mathbf{Q}_i=\mathbf{Q}$. This assumption holds true under the random-walk dynamic model if the temporal electron-density variance and correlations are constant. An approximation to $\mathbf{Q}$ is found by first estimating the state noise from the static reconstructions by computing the first-order differences,

$$\hat{\mathrm{v}}_i=\hat{\mathbf{x}}^{\mathrm{S}}_{i+1}-\hat{\mathbf{x}}^{\mathrm{S}}_i. \tag{10}$$

Algorithm 1 Ensemble Kalman Filter (see text for more information)

```
// Initialization
    $\{\tilde{\mathbf{x}}^1_{1|0},\dots,\tilde{\mathbf{x}}^l_{1|0},\dots,\tilde{\mathbf{x}}^L_{1|0}\}=$ IID_SAMPLE($\mathcal{N}(\mathbf{x}_0,\mathbf{\Pi}_0)$)
    $\mathbf{X}=[\tilde{\mathbf{x}}^1_{1|0}\dots\tilde{\mathbf{x}}^l_{1|0}\dots\tilde{\mathbf{x}}^L_{1|0}]$
    $\tilde{\mathbf{x}}_{1|0}=\frac{1}{L}\sum_{l=1}^{L}\tilde{\mathbf{x}}^l_{1|0}$

for $i=1,\dots,T$ do
    // Measurement Update
        $\mathbf{X}=\mathbf{X}-\tilde{\mathbf{x}}_{i|i-1}\mathbf{1}^T$
        $\mathbf{Z}=\frac{1}{L}[\mathbf{C}\circ(\mathbf{X}\mathbf{X}^T)]$
        $\mathbf{X}=\mathbf{X}+\tilde{\mathbf{x}}_{i|i-1}\mathbf{1}^T$
        $\mathbf{K}=\mathbf{Z}\mathbf{H}_i^T(\mathbf{H}_i\mathbf{Z}\mathbf{H}_i^T+\mathbf{R}_i)^{-1}$
        $\{\tilde{\mathbf{y}}^1_i,\dots,\tilde{\mathbf{y}}^l_i,\dots,\tilde{\mathbf{y}}^L_i\}=$ IID_SAMPLE($\mathcal{N}(\mathbf{y}_i,\mathbf{R}_i)$)
        $\mathbf{Y}=[\tilde{\mathbf{y}}^1_i\dots\tilde{\mathbf{y}}^l_i\dots\tilde{\mathbf{y}}^L_i]$
        $\mathbf{X}=\mathbf{X}+\mathbf{K}(\mathbf{Y}-\mathbf{H}_i\mathbf{X})$
        $\tilde{\mathbf{x}}_{i|i}=\frac{1}{L}\sum_{l=1}^{L}\mathbf{X}_{:,l}$

    if $i<T$ then
        // Model Evolution Update
            $\{\tilde{\mathbf{u}}^1_i,\dots,\tilde{\mathbf{u}}^l_i,\dots,\tilde{\mathbf{u}}^L_i\}=$ IID_SAMPLE($\mathcal{N}(\mathbf{0},\mathbf{Q}_i)$)
            $\mathbf{U}=[\tilde{\mathbf{u}}^1_i\dots\tilde{\mathbf{u}}^l_i\dots\tilde{\mathbf{u}}^L_i]$
            $\mathbf{X}=\mathbf{F}_i\mathbf{X}+\mathbf{U}$

    end if
end for
```

The nth element on the diagonal of $\mathbf{Q}$ is approximated as the temporal variance in the nth element of the state noise estimate $\hat{\mathrm{v}}_i$. Correlations in the state noise can also be approximated in this manner to determine the non-diagonal elements of $\mathbf{Q}$, but we found that a diagonal model for the state noise was sufficient to obtain the results in Section 4.

The remaining model parameters were chosen as follows. The spatial derivative matrix $\mathbf{D}$ is a first-order difference approximation to the derivative in both azimuth and elevation (but not radius). The same gradient operator is used as the spatial regularizer in the static and dynamic reconstructions. The EnKF initial-state mean $[\mathbf{x}_0]$ is the static estimate $[\hat{\mathbf{x}}_k^{\mathrm{S}}]$ at the time index k that corresponds to a half solar rotation relative to the first time index $i = 1$. The EnKF initial-state error covariance is $\mathbf{\Pi}_0 = \sigma^2 \mathbf{I}$. The initial-state error variance $[\sigma^2]$ was increased until the initial prior had only a minor impact on the final dynamic electron-density reconstruction. We found that $\sigma^2 = 10^{10}$ was sufficient to minimize the impact of the initial-state mean. Lastly, with the other parameters set, the regularization parameter λ was varied until the electron-density reconstruction was sufficiently smooth. We found that $\lambda = 1.6 \times 10^{-9}$ was a good choice for the static reconstructions and $\lambda = 1.0 \times 10^{-14}$ worked well in the dynamic case. An unsupervised approach to choosing these remaining model parameters could make use of methods such as cross validation (Golub, Heath, and Wahba, 1979; Butala, Frazin, and Kamalabadi, 2005).

4. Electron-Density Reconstruction

We now present tomographic reconstructions of electron density during February 2008 computed from COR1A and COR1B observations. The tomographic reconstructions are best when data are available over at least half a solar rotation. To satisfy this condition, all results are shown at dates after 14 February 2008. Each static reconstruction $\hat{\mathbf{x}}_i^{\mathrm{S}}$ required, on average, nearly 30 minutes of computation, while the complete dynamic reconstruction, *i.e.*, the computation of $\hat{\mathbf{x}}_i^{\mathrm{D}}$ at all time indices i, required about 40 minutes with an ensemble size $L = 32$.

Figure 1 shows a representative sample of spherical shell slices of the 3D electron-density reconstructions. Each spherical shell slice is a latitude *versus* longitude plot of reconstructed electron density at a constant radius of $1.7 R_{\odot}$. Each row of Figure 1 shows a COR1A static, COR1A dynamic, COR1B static, or COR1B dynamic electron-density reconstruction slice on three dates: 15 February 2008 00:05:00 UTC, 22 February 2008 00:05:00 UTC, and 29 February 2008 00:05:00 UTC.

We observe distinct changes in the structure of the streamer belt as a function of time in all four reconstructions in Figure 1. The static reconstructions tend to have larger, more connected, non-positive patches that seem to coalesce toward large areas near the poles. The non-positive patches in the dynamic reconstructions tend to cluster around the high-density regions in the streamer belt. These observations agree with the assertion in Kramar *et al.* (2009) that non-positive patches appear along high-density borders. Also, in general, the dynamic reconstructed density is lower, more spread out, and smoother than the static densities. The same effects would occur if the dynamic reconstructions were more significantly spatially regularized than the static reconstructions. This could also imply a larger dynamic relative residual, but this is not the case as discussed below.

In Figure 2, we see a 3D rendering of the coronal electron-density reconstructions on 25 February 2008 18:05:00 UTC. Each of the four reconstructions (COR1A static and dynamic and COR1B static and dynamic) are shown with two isosurfaces. The red isosurface is at a density of 2.5×10^6 N_{e} cm^{-3} and the blue isosurface shows non-positive patches

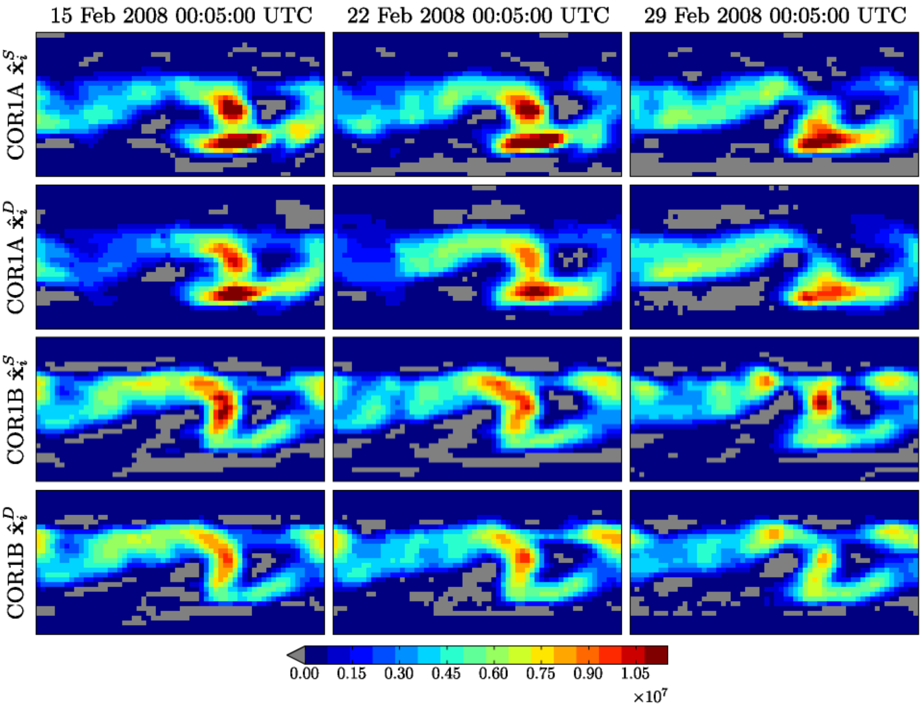

Figure 1 Two-dimensional spherical shell slices of reconstructed electron density at radius $1.7R_\odot$. Each column shows reconstructed electron density on a particular date. The first row shows the static reconstruction of the electron-density computed using COR1A pB measurements. The remaining rows show, in order, the dynamic COR1A, static COR1B, and dynamic COR1B electron-density reconstructions. The x- and y-axis of each image is the solar longitude and latitude, respectively, in units of degrees ranging from 0° to 360° in the x-direction and $-90°$ to 90° in the y-direction. The electron densities are shown on a common scale as indicated by the color-bar in the last row with units of N_e cm^{-3}. All non-positive densities are shown in gray.

of the reconstructed electron density. In this view, we can see the full 3D nature of the reconstructed electron density and visualize how the density structure extends throughout the reconstructed volume of the corona. When viewed in 3D, as opposed to 2D slices such as in Figure 1, it is clear that the higher densities are clustered near the Sun, while the non-positive density artifacts are more prominent near the outer boundary of the reconstructed corona. Also, it is clear that the non-positive artifacts are spatially much larger in the static reconstructions whereas the dynamic non-positive artifacts are smaller and less connected.

Figure 4 examines the agreement between the reconstructed electron density and the observed measurements in a plot of the relative residual defined as

$$r_i^{(\mathrm{S\ or\ D})} = \frac{\|\mathbf{y}_i - \mathbf{H}_i\,\hat{\mathbf{x}}_i^{(\mathrm{S\ or\ D})}\|_2}{\|\mathbf{y}_i\|_2}. \tag{11}$$

The relative residual compares the difference between a pB image and the estimate of that image computed from the forward model and an electron-density reconstruction. We note that a small residual indicates good agreement with the measurements but not necessarily good agreement between the reconstruction and the true electron density. Indeed, one major concern with the residual as a performance metric is that it must increase with the inclusion

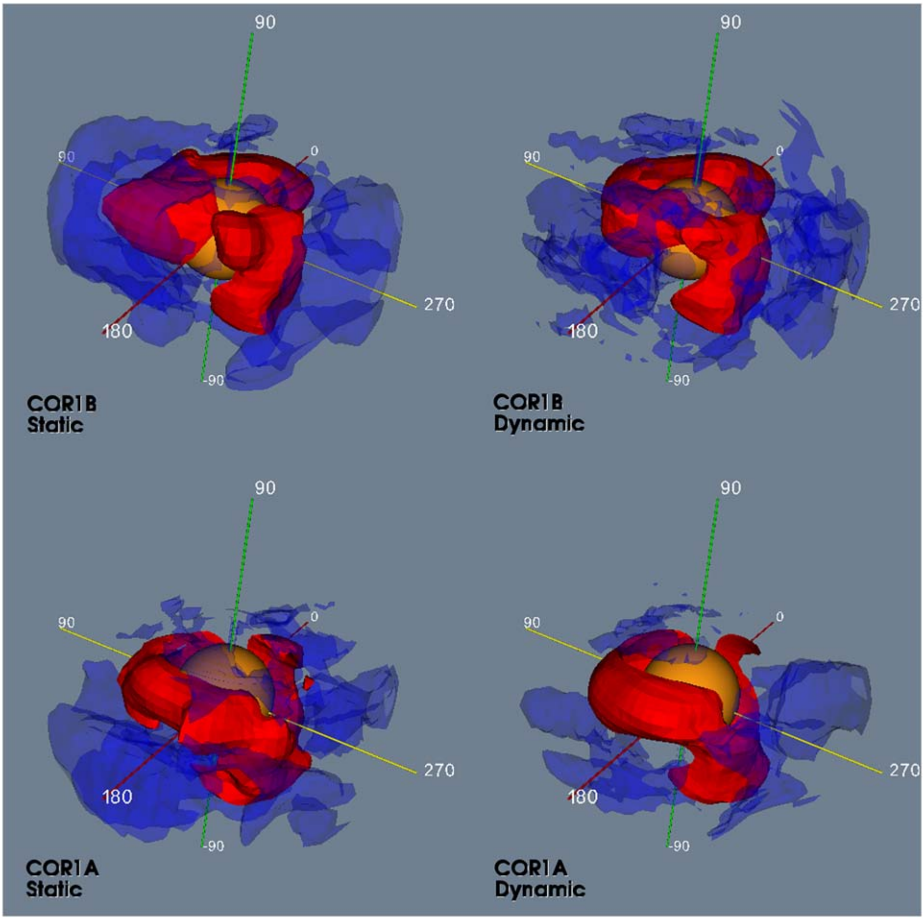

Figure 2 Three-dimensional isosurfaces of the four electron-density reconstructions on 25 February 2008 18:05:00 UTC. The red isosurface shows densities at $2.5 \times 10^6\ \mathrm{cm}^{-3}$. The translucent blue surface shows non-positive (non-physical) reconstructed densities. The central orange sphere has radius $1 R_\odot$ and represents the Sun.

of spatial regularization, but with the trade-off of reduced noise sensitivity and potentially better agreement between the reconstructions and the true coronal electron density (Demoment, 1989). This is exemplified in Figure 3, which compares the regularized and unregularized static electron-density reconstructions on 15 February 2008 00:05:00 UTC. We find that the regularized reconstruction is clearly more physically reasonable even though the unregularized reconstruction has a smaller residual. Ultimately, the relative residual shown in Figure 4 does not by itself provide definitive proof that the dynamic reconstruction algorithm produces more faithful electron-density reconstructions than the static approach. Instead, the reduction in the relative residual shown in Figure 4 coupled with the reduction in nonphysical artifacts discussed below provide evidence to support the conclusion that the dynamic method is better than the static method, but further study is required.

Alternatively, we could evaluate our approach in simulations where the true electron density is known. For reference, note that the static and dynamic approaches have been

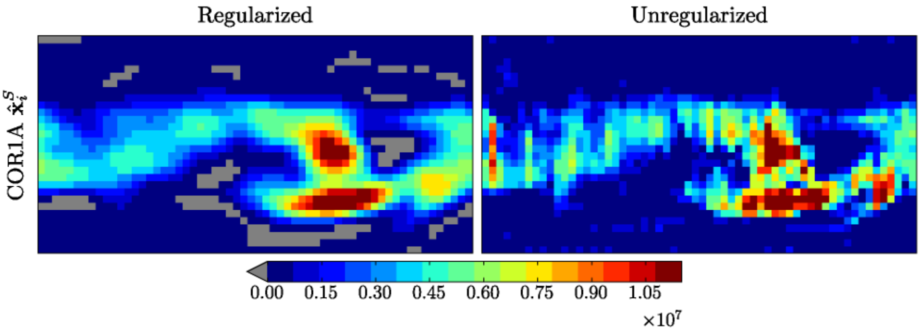

Figure 3 A spherical shell slice at radius $1.7R_\odot$ of the 15 February 2008 00:05:00 UTC COR1A static electron-density reconstruction with regularization (left) and with no regularization (right), *i.e.* a static reconstruction computed with $\lambda = 0$ in Equation (5). Note that the left image is a copy of the upper-left image in Figure 1 and is included for easy comparison to the unregularized reconstruction. Both images are shown on the same color scale. The relative residual of the regularized reconstruction is 0.239 and is 0.227 for the unregularized reconstruction.

previously evaluated and compared in numerical experiments including the simulated collapse of a magnetized molecular cloud (Frazin *et al.*, 2005), emergence of magnetic flux in the solar corona (Butala *et al.*, 2008), and diffusion (Butala *et al.*, 2009). In the context of this work, a more realistic and thus more compelling comparison of the static and dynamic approaches would consider a simulated time-dependent corona computed using hourly-updated magnetograms to drive a 3D magnetohydrodynamic solar-wind solution. However, the development of such numerical simulations is an ongoing research effort in the heliospheric-modeling community. Though not considered in this work, we plan to evaluate the dynamic and static reconstruction algorithms in more realistic coronal simulations once they are available.

With the above caveats, we now consider the relative residual in Figure 4. We see that the dynamic reconstruction typically has half the relative residual of the static reconstruction for both the COR1A and COR1B results. The reduction in the residual could be a result of decreased regularization. However, the results in Figure 1 and Figure 2 show that the dynamic and static reconstructions have similar qualitative smoothness. The dynamic and static reconstructions also have quantitatively similar smoothness, *i.e.* $\|\mathbf{D}\,\hat{\mathbf{x}}_i^{(\mathrm{S\ or\ D})}\|_2$ is 1.24×10^7 and 1.14×10^7 in the static and dynamic cases, respectively, for the time index i corresponding to 15 February 2008 00:05:00 UTC. In addition, the relative residual in the dynamic reconstructions are in fact smaller in comparison to the unregularized static reconstructions. These observations support the conclusion that differences in spatial regularization alone cannot explain the reduction in the dynamic residual. Further, for COR1B, there is a significant jump in the residual starting at 23 February 2008 18:05:00 UTC. Data outliers can cause such jumps, but they have been removed from the pB images prior to computing the electron-density reconstructions as discussed in Section 2. What is most surprising is that the COR1B dynamic relative residual also exhibits a jump starting at 23 February 2008 18:05:00 UTC, but it is much less pronounced. One difference between the static and dynamic reconstruction algorithms is that the dynamic method is provided with the measurement noise covariance $\mathbf{R}_i$, a measure of data quality. As a result, the dynamic method will be able to compensate for relatively poor quality measurements (assuming $\mathbf{R}_i$ is correct) that could severely distort the static electron-density reconstructions.

Interestingly, the results presented in the previous figures have shown that the EnKF produces fewer non-positive reconstructed densities than the static method. This can be seen

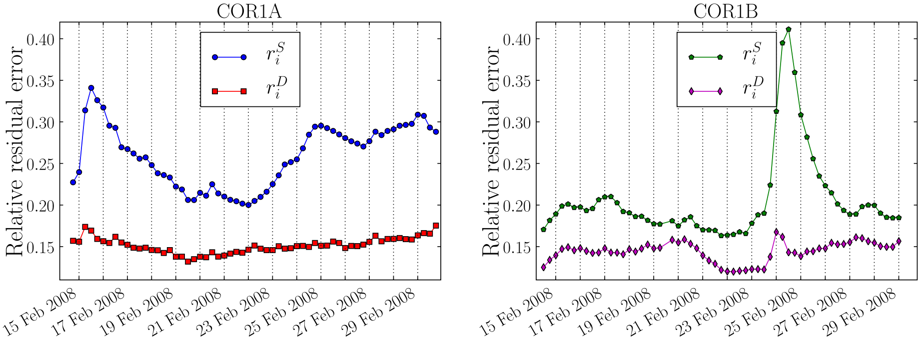

Figure 4 The relative static and dynamic residual (defined in Equation (11)) for the COR1A (left) and COR1B (right) electron-density reconstructions.

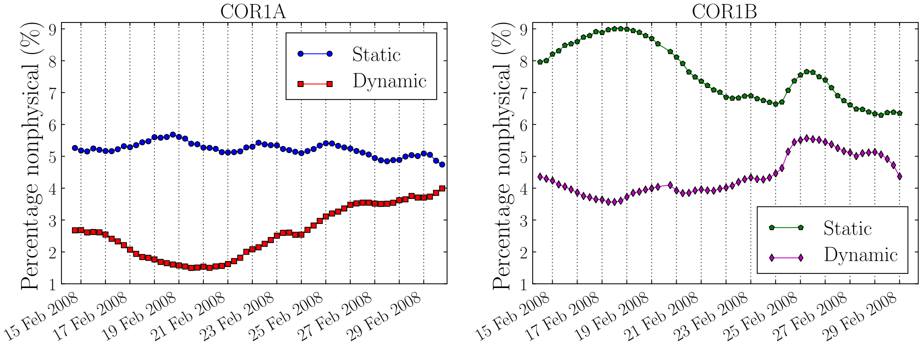

Figure 5 The percentage of non-positive reconstructed densities appearing in the COR1A (left) and COR1B (right) electron-density reconstructions.

in Figure 2, where the dynamic reconstructions have smaller volumes of non-positive artifacts. Figure 5 shows the percentage of non-positive voxels as a function of time in the four electron-density reconstructions. We find that the static reconstructions can have as many as twice the number of non-positive voxels. We emphasize that the dynamic reconstruction method produces a more physical result than the static method even though the dynamic algorithm does not constrain the electron density to be positive.

Figure 6 shows the average reconstructed density *versus* altitude above the Sun. The plot shows the reconstructed electron density averaged over a spherical shell slice (*i.e.*, a latitude *versus* longitude slice similar to those in Figure 1) at a given radius. All four reconstructions show a similar profile in the fall-off of the electron density with distance from the Sun, with the COR1A densities generally greater than the COR1B densities and static greater than dynamic. All four reconstructions increase in density at the largest altitudes, a reconstruction artifact common in tomographic imaging when the lines-of-sight extend to infinity and significant enough density exists outside of the finite reconstruction domain. On the other hand, there seems to be an artifact in the COR1A reconstructions at the lowest altitude not present, or just not as severe as, in the COR1B reconstructions. In addition, the electron-density reconstructions all decay linearly between about $1.7-2.2R_\odot$ on the $\log-\log$ plot with a fitted slope of about -6, indicating a clear power law in the fall-off rate of the average electron density *versus* distance from the Sun.

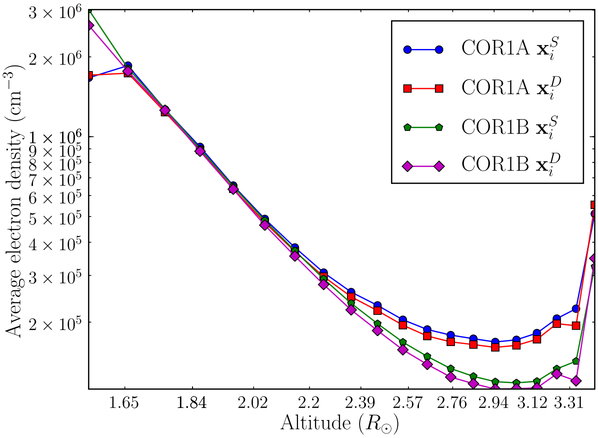

Figure 6 A log – log depiction of the reconstructed electron density *versus* the altitude above the Sun (an altitude of $1 R_\odot$ is at the photosphere). Each plotted point corresponds to the reconstructed electron density averaged over a spherical shell slice at a particular radius. As detailed in the legend, each curve in the figure is associated with a static or dynamic reconstruction (indicated by S or D) based either on COR1A or COR1B measurements.

5. Conclusions

This paper shows, for the first time, global 4D reconstructions of the coronal electron density. Our dynamic reconstruction method produces electron-density reconstructions that are superior to static reconstructions in several ways. First, while still present, the number of nonphysical densities is greatly reduced. In addition, the dynamic reconstructions appear qualitatively better, exhibiting a generally smoother and more connected, *i.e.* more physically reasonable, reconstructed streamer belt. Finally, these benefits come without a significant increase in computational cost and, in fact, the full dynamic reconstruction required less computation than the sequence of static reconstructions.

Several future research directions are immediately suggested by the work presented in this paper. For one, we have so far considered COR1A and COR1B separately, but tomography improves with additional simultaneous vantage points. A forthcoming paper will address intercalibration issues between COR1A and COR1B and present 4D electron-density reconstructions based on both data sets simultaneously, perhaps combining data from additional coronagraphs depending on further intercalibration issues. Second, the random-walk dynamic model is certainly not the best possible choice for solar tomography. The first step would be to consider the effects of differential rotation, which can be incorporated as a spatially-varying rotation in the state dynamic model $\mathbf{F}_i$. However, after a number of studies, it is still unclear how the rotation rate depends on latitude and height (Giordano and Mancuso, 2008). We are also currently working towards incorporating MHD physics into our dynamic reconstruction framework. A better dynamic model will improve our 4D electron-density estimates and, ultimately, enable forecasting of the future electron-density state in the solar corona. Further, the solar magnetic field strongly influences the coronal electron density. Models for the solar magnetic-field structure could be a powerful means to further constrain our dynamic tomographic electron-density reconstructions (Wiegelmann and Inhester, 2003).

Acknowledgements This work was supported in part by the National Science Foundation under Grants 055561 SHINE and 0620550 CMG, by NASA under Grant NNG-04GG32G to the University of Illinois and under NASA GSRP fellowship NNX08AT43H FLL.

References

Aschwanden, M.J.: 2004, *Physics of the Solar Corona*, Springer, Berlin.

Barbey, N., Auchère, F., Rodet, T., Vial, J.C.: 2008, A time-evolving 3D method dedicated to the reconstruction of solar plumes and results using extreme ultraviolet data. *Solar Phys.* **248**, 409 – 423.

Butala, M.D., Frazin, R.A., Kamalabadi, F.: 2005, Three-dimensional estimates of the coronal electron density at times of extreme solar activity. *J. Geophys. Res.* **110**, A09S09. doi:10.1029/2004JA010938.

Butala, M.D., Kamalabadi, F., Frazin, R.A., Chen, Y.: 2008, Dynamic tomographic imaging of the solar corona. *IEEE J. Sel. Top. Signal Process.* **2**, 755 – 766.

Butala, M.D., Frazin, R.A., Chen, Y., Kamalabadi, F.: 2009, Tomographic imaging of dynamic objects with the ensemble Kalman filter. *IEEE Trans. Image Process.* **18**, 1573 – 1587.

Cohen, O., Sokolov, I.V., Roussev, I.I., Arge, C.N., Manchester, W.B., Gombosi, T.I., Frazin, R.A., Park, H., Butala, M.D., Kamalabadi, F., Velli, M.: 2007, A semiempirical magnetohydrodynamical model of the solar wind. *Astrophys. J. Lett.* **654**, 163 – 166.

Davila, J.M.: 1994, Solar tomography. *Astrophys. J.* **423**, 871 – 877.

Demoment, G.: 1989, Image reconstruction and restoration: Overview of common estimation structures and problems. *IEEE Trans. Acoust. Speech Signal Process.* **37**(12), 2024 – 2036.

Dunn, T., Jackson, B.V., Hick, P.P., Buffington, A., Zhao, X.P.: 2005, Comparative analysis of the CSSS calculation in the UCSD tomographic solar observations. *Solar Phys.* **227**, 339 – 353.

Evensen, G.: 1994, Sequential data assimilation with a nonlinear quasi-geostrophic model using Monte Carlo methods to forecast error statistics. *J. Geophys. Res.* **99**, 10143 – 10162.

Evensen, G.: 2003, The ensemble Kalman filter: theoretical formulation and practical implementation. *Ocean Dyn.* **53**, 343 – 367.

Frazin, R.A., Kamalabadi, F.: 2005, Rotational tomography for 3D reconstruction in the post-SOHO era. *Solar Phys.* **228**, 219 – 237.

Frazin, R.A., Butala, M.D., Kemball, A., Kamalabadi, F.: 2005, Time-dependent reconstruction of nonstationary objects with tomographic or interferometric measurements. *Astrophys. J. Lett.* **635**, L197 – L200.

Giordano, S., Mancuso, S.: 2008, Coronal rotation at solar minimum from UV observations. *Astrophys. J.* **688**, 656 – 668.

Golub, G.H., Heath, M., Wahba, G.: 1979, Generalized cross-validation as a method for choosing a good ridge parameter. *Technometrics* **21**(2), 215 – 223.

Howard, R.A., Moses, J.D., Vourlidas, A., Newmark, J.S., Socker, D.G., Plunkett, S.P., Korendyke, C.M., Cook, J.W., Hurley, A., Davila, J.M., Thompson, W.T., St. Cyr, O.C., Mentzell, E., Mehalick, K., Lemen, J.R., Wuelser, J.P., Duncan, D.W., Tarbell, T.D., Wolfson, C.J., Moore, A., Harrison, R.A., Waltham, N.R., Lang, J., Davis, C.J., Eyles, C.J., Mapson-Menard, H., Simnett, G.M., Halain, J.P., Defise, J.M., Mazy, E., Rochus, P., Mercier, R., Ravet, M.F., Delmotte, F., Auchere, F., Delaboudinière, J.P., Bothmer, V., Deutsch, W., Wang, D., Rich, N., Cooper, S., Stephens, V., Maahs, G., Baugh, R., McMullin, D., Carter, T.: 2008, Sun Earth connection coronal and heliospheric investigation (SECCHI). *Space Sci. Rev.* **136**, 67 – 115.

Johns, C.J., Mandel, J.: 2008, A two-stage ensemble Kalman filter for smooth data assimilation. *Environ. Ecol. Stat.* **15**, 101 – 110.

Kailath, T., Sayed, A.H., Hassibi, B.: 2000, *Linear Estimation*, Prentice-Hall, Upper Saddle River.

Kaiser, M.L., Kucera, T.A., Davila, J.M., St. Cyr, O.C., Guhathakurta, M., Christian, E.: 2007, The STEREO mission: An introduction. *Space Sci. Rev.* **136**, 5 – 16.

Kalman, R.E.: 1960, A new approach to linear filtering and prediction problems. *J. Basic Eng., Trans. ASME* **82**, 35 – 45.

Kramar, M., Jones, S., Davila, J., Inhester, B., Mierla, M.: 2009, On the tomographic reconstruction of the 3D electron density for the solar corona from STEREO COR1 data. *Solar Phys.* **259**, 109 – 121.

Thompson, W.T., Reginald, N.L.: 2008, The radiometric and pointing calibration of SECCHI COR1 on STEREO. *Solar Phys.* **250**, 443 – 454.

Thompson, W.T., Davila, J.M., Fisher, R.R., Orwig, L.E., Mentzell, J.E., Hetherington, S.E., Derro, R.J., Federline, R.E., Clark, D.C., Chen, P.T., Tveekrem, J.L., Martino, A.J., Novello, J., Wesenberg, R.P., St. Cyr, O.C., Reginald, N.L., Howard, R.A., Mehalick, K.I., Hersh, M.J., Newman, M.D., Thomas, D.L., Card, G., Elmore, D.: 2003, The COR1 inner coronagraph for STEREO-SECCHI. *Proc. SPIE* **4853**, 1 – 11.

van de Hulst, H.C.: 1950, The electron density of the solar corona. *Bull. Astron. Inst. Neth.* **11**(410), 135 – 150.

Vásquez, A.M., Frazin, R.A., Hayashi, K., Sokolov, I.V., Cohen, O., Manchester, W.B. IV, Kamalabadi, F.: 2008, Validation of two MHD models of the solar corona with rotational tomography. *Astrophys. J.* **682**, 1328 – 1337.

Wiegelmann, T., Inhester, B.: 2003, Magnetic field modeling and tomograph: First steps towards a consistence reconstruction of the solar corona. *Solar Phys.* **214**, 287 – 312.

Zhang, Y., Ghodrati, A., Brooks, D.H.: 2005, An analytical comparison of three spatio-temporal regularization methods for dynamic linear inverse problems in a common statistical framework. *Inverse Probl.* **21**, 357 – 382.